RSC Medicinal Chemistry

ROYAL SOCIETY OF CHEMISTRY

RESEARCH ARTICLE

View Article Online
View Journal | View Issue

Cite this: *RSC Med. Chem.*, 2023, **14**, 1767

First-in-class small molecule inhibitors of ICOS/ICOSL interaction as a novel class of immunomodulators†

Somaya A. Abdel-Rahman,[ab] Katarzyna Świderek[c] and Moustafa T. Gabr *[a]

The interaction of the inducible co-stimulator (ICOS) with its ligand (ICOSL) plays key roles in T-cell differentiation and activation of T-cell to B-cell functions. The ICOS/ICOSL pathway is a validated target for T-cell lymphomas induced by the proliferation of T-follicular helper (Tfh) cells. Moreover, the inhibition of ICOS/ICOSL interaction can decrease the enhancement of immunosuppressive regulatory T cells (Tregs) in both hematologic malignancies and solid tumors. However, targeting ICOS/ICOSL interaction is currently restricted to monoclonal antibodies (mAbs) and there are no small molecules in existence that can block ICOS/ICOSL. To fill this gap, we report herein the first time-resolved fluorescence resonance energy transfer (TR-FRET) assay to evaluate the ability of small molecules to inhibit ICOS/ICOSL interaction. Implementation of the developed TR-FRET assay in high-throughput screening (HTS) of a focused chemical library resulted in the identification of **AG-120** as a first-in-class inhibitor of ICOS/ICOSL interaction. We further employed docking studies and molecular dynamics (MD) simulations to identify the plausible mechanism of blocking ICOS/ICOSL complex formation by **AG-120**. Using the structure–activity relationship (SAR) by catalog approach, we identified **AG-120-X** with an IC_{50} value of 4.68 ± 0.47 μM in the ICOS/ICOSL TR-FRET assay. Remarkably, **AG-120-X** revealed a dose-dependent ability to block ICOS/ICOSL interaction in a bioluminescent cellular assay based on co-culturing Jurkat T cells expressing ICOS and CHO-K1 cells expressing ICOSL. This work will pave the way for future drug discovery efforts aiming at the development of small molecule inhibitors of ICOS/ICOSL interaction as potential therapeutics for cancer as well as other diseases.

Received 29th March 2023,
Accepted 28th July 2023

DOI: 10.1039/d3md00150d

rsc.li/medchem

Introduction

The therapy landscape for various types of cancers has been transformed by immune checkpoint blockade (ICB).[1–5] However, the response to ICB is limited as a significant number of cancer patients either do not respond to it or experience only temporary effects due to resistance that is either inherent or acquired. Potential contributors to ICB resistance include cell-intrinsic mechanisms as well as extrinsic factors from the tumor microenvironment (TME).[6–9] These factors include the upregulation of other immune checkpoints and the presence of tumor-infiltrating Tregs that negatively affect the response to ICB.[6–9] Combination approaches based on targeting multiple negative immune checkpoints have been pursued in clinical studies to maximize the efficacy of ICB.[10–12] Targeting co-stimulatory immune checkpoints is another promising approach in promoting antitumor T-cell function and overcoming ICB resistance.[13–18] However, targeting co-stimulatory checkpoints with monoclonal antibodies (mAbs) has resulted in side effects that hinder their clinical translation.[19] Therefore, research efforts are currently directed toward the development of efficient therapeutic strategies targeting co-stimulatory receptors that would enable the management of side effects.

Given the intricate nature of the TME, the combination of mAbs targeting immune checkpoints with small molecule agonists/inhibitors has emerged as a powerful approach to maximize the number of patients benefiting from ICB.[20] However, all FDA-approved therapeutics targeting immune checkpoints are mAbs, which entails a major limitation for the development of an effective combination of therapeutic modalities for cancer patients. In general, there are several disadvantages to mAbs as a therapeutic modality, such as suboptimal tumor penetration, high costs of manufacturing, and potential immunogenicity.[21–24] Importantly, mAbs

[a] *Department of Radiology, Molecular Imaging Innovations Institute (MI3), Weill Cornell Medicine, New York, NY 10065, USA. E-mail: mog4005@med.cornell.edu*
[b] *Department of Medicinal Chemistry, Faculty of Pharmacy, Mansoura University, Mansoura 35516, Egypt*
[c] *BioComp Group, Institute of Advanced Materials (INAM), Universitat Jaume I, 12071 Castellon, Spain*

† Electronic supplementary information (ESI) available: Experimental procedures and supplementary figures. See DOI: https://doi.org/10.1039/d3md00150d

generally possess prolonged half-lives, which potentially result in long-term on-target mediated immune-related adverse events (irAEs) that can be fatal.[25,26] In comparison to mAbs, small molecules possess oral bioavailability and enhanced tumor penetration.[27,28] Remarkably, small molecules are more amenable to pharmacokinetic optimization, which allows adopting flexible dosage regimens that may enable avoiding irAEs associated with mAbs. On the other hand, the off-target effects of small molecules can result in severe side effects, and the potency of numerous small molecules may not match that of mAbs.

Inducible T cell co-stimulator (ICOS) is a receptor that acts as a co-stimulator to enhance T-cell responses against foreign antigens.[29,30] ICOS is expressed on T lymphocytes as well as a variety of T cell subsets.[31,32] ICOS signaling is initiated upon engagement by its ligand, ICOSL, which is expressed on antigen-presenting cells (APCs), including macrophages, dendritic cells (DCs), and B-cells.[33,34] Inhibition of ICOS/ICOSL interaction represents a powerful immunotherapeutic approach for cancer therapy. This can be achieved by suppressing immunosuppressive Tregs or by blocking T-follicular helper (Tfh)-cell differentiation (Fig. 1). The presence of Tregs has been detected in the TME of many human cancers and is usually associated with poor prognosis.[35–37] The ICOS/ICOSL pathway plays key roles in generating Tregs as well as promoting the immunosuppressive functions of Tregs.[38–40] ICOS is highly expressed by tumor-associated Tregs in several types of cancer, including breast cancer and melanoma.[41–44] ICOSL is expressed by plasmacytoid DCs (pDCs) in breast,[42] ovarian,[45] and gastric cancers.[46] The interaction between pDCs and Tregs through ICOS/ICOSL interaction favors the expansion and survival of Tregs. Moreover, ICOS/ICOSL interaction promotes the survival and immunosuppressive function of Tregs through nuclear factor of activated T cell (NFAT) activation.[47] Small molecule inhibitors of ICOS/ICOSL interaction will impede the interaction between pDCs and Tregs through ICOS/ICOSL engagement (Fig. 1A). The implication of ICOS/ICOSL interaction in promoting the immunosuppressive functions of Tregs in several solid tumors would render small molecules with effective tumor penetration ability as promising cancer immunotherapies.

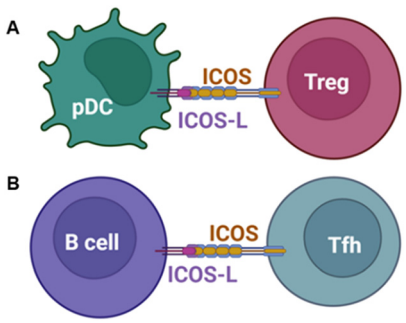

Fig. 1 Opportunities for inhibitors of ICOS/ICOSL interaction in cancer immunotherapy. (A) Inhibition of the expansion of immunosuppressive Tregs. (B) Blocking ICOS-mediated Tfh-cell differentiation.

The interaction between ICOS and ICOSL on T and B cells is crucial in positively regulating the proliferation of Tfh cells in the late stage (Fig. 1B).[32] ICOS signaling is responsible for persistent T-cell migration at the boundary between the T-cell zone and the B-cell follicle *in vivo*.[48] Remarkably, the presence of ICOSL on B cells serves as a molecular bridge linking the dynamics of T cell-B cell interactions and is essential in sustaining engagement between Tfh cells and B cells within germinal centers (GCs).[49] Reduced ICOSL expression on follicular bystander B cells hinders the development of Tfh cells and optimal GC responses.[48] Angioimmunoblastic T-cell lymphoma (AITL) and peripheral T-cell lymphoma with T follicular helper phenotype (PTCL-Tfh) are a group of complex clinicopathological conditions that arise from the expansion of Tfh cells exhibiting high expression levels of ICOS.[50–54] Targeting ICOS expressed on the surface of Tfh cells has emerged as a promising therapeutic strategy for T-cell lymphomas. In this context, MEDI-570, an anti-ICOS antagonist mAb currently being evaluated in a phase I clinical trial for T-cell lymphomas (NCT02520791), showed promising clinical activity in poor-risk refractory and heavily pretreated AITL.[55] Given the severe prognosis of T-cell lymphomas, there is an urgent need for newer agents targeting specific molecular hallmarks of these disease entities that may represent a rational approach to improve the treatment for patients with relapsed/refractory PTCL and AITL.[56] Therefore, the establishment of targeting ICOS/ICOSL interaction with small molecules would represent a promising new immunotherapeutic strategy for T-cell lymphomas.

Results and discussion

In continuation of our efforts in establishing and implementing luminescence-based assays that can be utilized for high-throughput screening (HTS),[57] we developed the first time-resolved fluorescence resonance energy transfer (TR-FRET) assay for HTS of small molecules for ICOS/ICOSL inhibition (Fig. 2). TR-FRET involves the use of a pair of fluorescent molecules, known as a donor and an acceptor dye. These dyes transfer energy to each other when they are in close proximity. Aiming to identify the best acceptor–donor pairs for the ICOS/ICOSL interaction, we explored ICOS : ICOSL cross-titration with different tags *versus* multiple combinations of donor and acceptor reagents. The largest signal ratio was detected upon using the Tb cryptate labeled anti-His Ab as the donor and XL665 labeled anti-human Ab as the acceptor (Fig. 2) with a ratio of 1 : 10. The signal to background (S/B) ratio was 12.4. Optimized conditions for maximizing the signal ratio involved final concentrations of 10 nM for both human Fc-tagged ICOS and His-tagged ICOSL. Titration of XL665-labeled ICOS to Tb-labeled ICOSL illustrated the FRET efficiency based on the hyperbolic dependence of the TR-FRET ratio on the acceptor

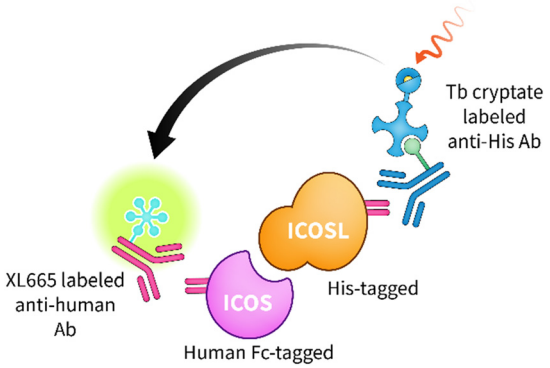

Fig. 2 Schematic illustration of the TR-FRET assay developed to identify small molecules that inhibit ICOS/ICOSL interaction.

concentration (Fig. S1, ESI†). Molecules that can block ICOS/ICOSL interaction would consequently result in an attenuated TR-FRET signal. Remarkably, a concentration-dependent decrease in the TR-FRET ratio was detected in the presence of varying concentrations of an anti-ICOS mAb (Fig. S2, ESI†). The validity of the assay for HTS has been demonstrated with a mean Z' factor of 0.89 ± 0.07, revealing a high-quality assay for HTS. The Z' factor corresponds to the ratio of data signal variability (standard deviation) to dynamic range (*i.e.*, change in TR-FRET signal for positive and negative controls).[58]

We established a chemical library (~3000 compounds) with diversified chemical structures. Our library entailed compounds from the NCI Diversity Set VII, FDA-approved drugs, bioactive compounds from APExBIO, Discovery Diversity Set from Enamine, and CORE library stock from ChemBridge. Notably, the characteristics of this library comply with Lipinski's rule of Five, a valuable parameter for evaluating drug-likeness of small molecules based on their physicochemical properties.[59] Moreover, we removed promiscuous compounds from our diversified chemical library using the PAINS (Pan-Assay Interference Compounds) filter.[60] Initially, we subjected our chemical library to single-dose (50 μM) screening using our developed TR-FRET assay for ICOS/ICOSL interaction. Agents that block the interaction between both proteins result in an attenuated TR-FRET signal. Hits were identified by the ability to decrease the TR-FRET signal by more than 5 standard deviations (5 SD) lower than the total mean. **AG-120** (Fig. 3A) exhibited remarkable attenuation of the TR-FRET signal (>90%) of ICOS/ICOSL in comparison to the identified hits. Dose-dependent TR-FRET screening was conducted for **AG-120**, which revealed a half maximal inhibitory concentration (IC_{50}) value of 12.24 ± 0.87 μM (Fig. 3B). It is worth mentioning that evaluation of **AG-120** for ICOS/ICOSL inhibition using a commercially available ELISA-based ICOS/ICOSL inhibitor screening assay from BPS Bioscience (Catalog #79673) indicated an IC_{50} value of 10.32 ± 0.41 μM (Fig. S3, ESI†). The close agreement between the outcome of the ELISA-based ICOS/ICOSL inhibition assay and our developed TR-FRET assay validates **AG-120** as a first-in-class small molecule inhibitor of ICOS/ICOSL interaction.

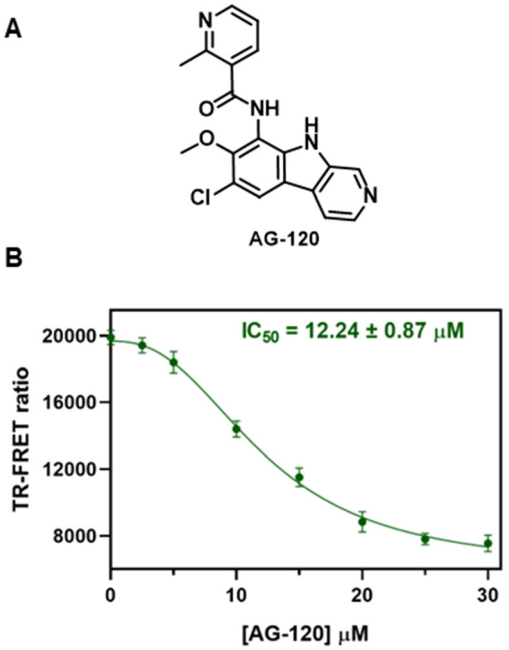

Fig. 3 (A) Chemical structure of **AG-120**. (B) Dose–response curve of **AG-120** in TR-FRET assay of ICOS/ICOSL. Error bars represent standard deviation (n = 3).

The ICOS/ICOSL complex is a challenging system from a computational point of view because the interface between both proteins involves not only protein–protein but also protein–*N*-glycan interactions. As identified by Julien and co-workers[61] and as shown in Fig. 4A, based on the analysis of crystal structure, two main recognition areas for the ICOS–ICOSL complex formation can be identified. In the first, amino acids between $_{66}$TKTKGS$_{71}$ and $_{114}$FDPPPFK$_{120}$ in ICOS, with the special indication to Phe114 and Phe119 as well as Gln50, whose mutations drastically reduced the ICOSL affinity towards ICOS,[62] interact by H-bonding and aromatic stacking with residues from strands C and C′ and loops CC′ and C′D of ICOSL. In the second region, N110-glycan of ICOS, which consists of two *N*-acetyl glucosamine (GlcNAc) and three mannose residues, forms H-bond interactions with Phe122, Gln123, and Glu124 of ICOSL, and it is believed that it sterically gates ICOSL binding. Therefore, it is expected that restricting access to described key residues may contribute to blocking the possibility of ICOS–ICOSL complex formation.

To elucidate the possible mechanism, according to which **AG-120** operates and blocks ICOS/ICOSL complex formation, computational chemistry tools were employed. At first, blind docking studies were done to establish potential ligand-binding sites, separately for ICOS and ICOSL proteins (for details see the Experimental section). Four poses generated by docking software with the computed values of the highest affinity were analyzed. As shown in Fig. 4B, the highest-scored binding pose in the proximity of the ICOS/ICOS-L interface was identified only in the case of the ICOS protein, suggesting that **AG-120** can establish weak interactions with

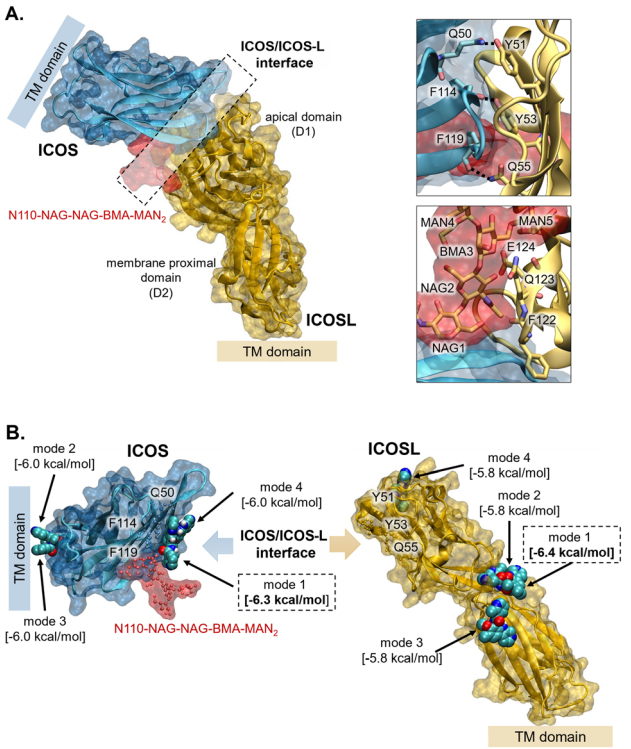

Fig. 4 ICOS/ICOSL structures. (A) ICOS/ICOSL complex with highlighted key residues for interactions formed at the ICOS/ICOSL interface. The structure of ICOS is shown in blue, ICOSL is shown in yellow, and the N110–NAG–NAG–BMA–MAN2 oligosaccharide chain is shown in red. (B) The highest-scored position of **AG-120** in ICOS and ICOSL obtained in docking studies. Values provided in brackets correspond to binding affinity determined based on the scoring function.

the surface despite no singular binding cavity being characterized in this region. On the contrary, the same molecule never occupies the ICOS/ICOSL interface region in the ICOSL structure, which suggests a lack of complementarity between this area and the architecture of the inhibitor. Consequently, this result suggests that the presence of the inhibitor in the $_{114}$FDPPPFK$_{120}$ region of ICOS provides an important hindrance for ICOS–ICOSL complex formation. On the other hand, docking results indicated that the best binding site for this inhibitor in ICOSL protein is located at the interface formed between the apical (D1) and membrane proximal (D2) domains. Nevertheless, we assume that this position of **AG-120** would not affect ICOS–ICOSL complex formation, considering its significantly large distance from the ICOS/ICOS-L interface. In the case of ICOS, a second binding location was found, as indicated in Fig. 4B by modes 2 and 3. This binding location would be however unavailable when ICOS is attached to a transmembrane (TM) domain that is formed between positions 140–161 and can be also ignored.

Therefore, in its most favorable pose in ICOS protein (mode 1 shown in Fig. 4B with the affinity of −6.3 kcal mol^{-1} according to docking studies), **AG-120** establishes three pi–pi stacking interactions with Phe114 as well as three conventional hydrogen bond interactions, two of them with two consecutive NAG1 and NAG2 residues of oligosaccharide and one with Lys52. Additionally, one carbon–hydrogen bond was identified, formed between the inhibitor and Gln50. All established interactions in docking studies are illustrated in Fig. S5 of the ESI† and suggest that **AG-120** occupies the most critical position that would restrict access of ICOSL to this region. Nevertheless, it must be pointed out that the present docking simulations assume the rigidness of the protein and do not necessarily reflect the real behavior of the newly formed complex. Therefore, to ensure our prediction, molecular dynamics (MD) simulations were done to explore more realistic interactions established between the inhibitor and the ICOS/ICOSL interface region that can be changed due to the plasticity of the enzyme.[63] After exploration of three replicas of NTP MD simulations at 300 K, it was observed that during all simulations the ligand remains around the region of ICOS that corresponds to the ICOS/ICOSL interface, *i.e.*, in proximity to Phe114 and Phe119, as well as N110-glycan, as shown in Fig. 5A and B. Curiously, the behavior of the molecule does not suggest that there is one specific binding place in this area, but rather the molecule of inhibitor constantly explores alternative poses in this region following conformational changes experienced by the N110-glycan. Due to the high flexibility of this long glycan chain, the position of the molecule is evolving, as it is illustrated in Fig. 5A and demonstrated by the movie deposited in the ESI† presenting the free MD trajectories. Probably such a highly dynamic behavior of the ligand and N110 glycan can explain why rather a weak binding of this molecule was determined experimentally for ICOS protein. It must be however commented that analysis of the results from MD simulations focused on the evolution of a distance between the center of mass computed for the position of heavy atoms of the inhibitor and key residues revealed that for most of the time the inhibitor stays in close contact with the N110-glycan and area of ICOS corresponding to the

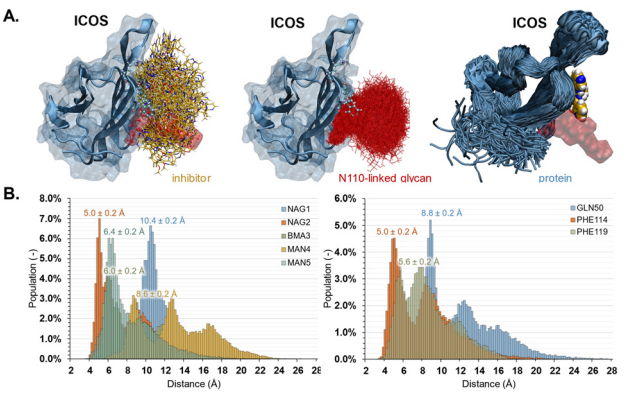

Fig. 5 Results of 300 ns of NPT-MD simulations of the ICOS–inhibitor complex. (A) Fluctuation of the inhibitor, N110-glycan, and protein during MD simulations. (B) Distribution of distances between the center of mass of the inhibitor and residues of N110-glycan and ICOS key residues from the ICOS/ICOSL interface. Results are based on 30 000 snapshots.

ICOS–ICOSL interface, as shown in Fig. 5B. Especially crucial for inhibitor binding appeared to be the presence of glycan residues, 2-acetamido-2-deoxy-beta-D-glucopyranose (NAG2) and beta-D-mannopyranose in position 3 (BMA3) and 5 (MAN5) as well as Phe114 and Phe119 amino acids.

Contact analysis revealed the existence of several hydrogen bond interactions formed during MD simulations. The most frequently appearing are those in which O29 of **AG-120** serves as an H-bond acceptor, while N19 plays the role of the donor (for atom numbering see the ESI†). The oxygen atom of **AG-120** is mostly involved in H-bond interactions with H_3O of NAG2 and H_2O of BMA3, whereas N19 forms interactions with O_2N of NAG2. The remaining contacts as ones created between **AG-120** and Phe114 and Phe119 originate from pi–pi stacking interactions.

Results obtained applying molecular docking and MD simulation techniques agree with experimental observations showing that **AG-120** can serve as an inhibitor of ICOS–ICOSL complex formation. As revealed by computational studies, this is achieved due to weak but long-time interactions created between **AG-120** and the main region of the ICOS responsible for the recognition of its primary ligand (ICOSL).

The structure–activity relationship (SAR) by catalog is an established approach to investigate the impact of structural variations in identified hits from screening platforms on the desired biological activity.[64–66] This approach relies on purchasing structural analogs of the desired hit compounds from commercial sources. Therefore, we procured a panel of structural analogs of **AG-120** from commercial sources and evaluated the ability of these structural analogs to inhibit ICOS/ICOSL interaction using our developed TR-FRET assay (Table 1). The aim of this study was to determine the essential structural features in **AG-120** for ICOS/ICOSL inhibition and explore chemical space that would result in maximizing the potency of **AG-120** as an ICOS/ICOSL inhibitor. As shown in Table 1, a structural analog of **AG-120** that lacks the methoxy group (**AG-120-I**) maintained ICOS/ICOSL inhibitory activity (IC_{50} = 13.89 ± 0.58 μM). However, variations in the 3-pyridine carboxamide moiety of **AG-120** *via* the introduction of linkers (**AG-120-II**), substituted phenyl moieties (**AG-120-III**, **AG-120-IV**, **AG-120-VI**, and **AG-120-VII**), or the incorporation of pyridinyl isomers (**AG-120-V** and **AG-120-VIII**) have resulted in a remarkable loss in ICOS/ICOSL inhibitory activity. Such an effect was partially abolished upon the incorporation of a benzylamino fragment to a structural analog of **AG-120** bearing a 2-pyridine carboxamide moiety (**AG-120-IX**). Based on this outcome, we further screened a structural analog of **AG-120** bearing a 3-pyridine carboxamide moiety and a benzylamino fragment (**AG-120-X**). As shown in Table 1, **AG-120-X** was the most potent ICOS/ICOSL inhibitor identified from this study with an IC_{50} value of 4.68 ± 0.47 μM. Consistent with our SAR studies, a structural analog of **AG-120-X** bearing a 2-pyridine carboxamide moiety (**AG-120-XI**) possessed a reduced ICOS/ICOSL inhibitory activity in comparison to **AG-120-X**. It is worth mentioning that other structural analogs of **AG-120** with alternative substitution patterns (**AG-120-XII**, **AG-120-XIII**, and **AG-120-XIV**) revealed minimal ICOS/ICOSL inhibitory activity (Table 1). Notably, variations in the 3-pyridine carboxamide moiety of **AG-120** by introducing a pyrimidyl derivative resulted in the most pronounced enhancement in the ICOS/ICOSL inhibitory activity (**AG-120-XV**). On the other hand, variations in the 3-pyridine carboxamide moiety *via* incorporating saturated heterocycles had minimal impact on the ICOS/ICOSL inhibitory activity (**AG-120-XVI**). The outcome of our SAR studies will guide further efforts aiming at the development of small molecule inhibitors of ICOS/ICOSL interaction.

We further evaluated the ability of our top hit compound, **AG-120-X**, to block ICOS/ICOSL interaction in a cell-based assay. For this, we implemented a bioluminescent cell-based assay from Promega (Catalog #JA6001), which is designed to evaluate the ability to block ICOS/ICOSL interaction. The assay consists of two genetically engineered cell lines: (1) Jurkat T cells that endogenously express TCR/CD3 and are engineered to express human ICOS and a NanoLuc® (NL) luciferase reporter driven by ICOS and TCR/CD3 pathway-dependent response elements and (2) CHO-K1 cells expressing an engineered cell surface protein designed to activate TCR/CD3 in an antigen-independent manner and ICOSL. When the two cell types are co-cultured, ICOSL cells activate TCR/CD3 and ICOS on the ICOS effector cells to induce maximum promoter-mediated luminescence. As shown in Fig. 6, the dose-dependent reduction in the luminescence in co-cultures of ICOS effector cells and ICOSL/CHO-K1 cells upon incubation with multiple concentrations (5, 10, and 20 μM) of **AG-120-X** validates the ability of **AG-120-X** to block ICOS/ICOSL interaction between two different cell types. In this assay, we used anti-ICOS mAb as a positive control (Fig. 6). Notably, our preliminary *in vitro* pharmacokinetic profiling of **AG-120-X** revealed its metabolic stability (in human plasma, simulated fluids, and rat liver microsomes) as well as negligible cytotoxicity against HEL 299 cells (Table S2†). Thus, **AG-120-X** represents a promising lead for further optimization for screening in established animal models for ICOS/ICOSL inhibition.

Conclusions

In summary, we have developed and optimized the first TR-FRET screening assay to identify small molecule inhibitors of ICOS/ICOSL interaction. Implementation of the developed assay in screening a chemical library with diversified structures resulted in the discovery of **AG-120** as a first-in-class inhibitor of ICOS/ICOSL interaction. We employed the SAR by catalog approach to identify the essential structural features in **AG-120** for the ICOS/ICOSL inhibitory profile. Remarkably, our approach resulted in the identification of **AG-120-X** with ~3-fold enhancement in the ICOS/ICOSL inhibitory profile in comparison to **AG-120** as well as functional activity in cellular assays. Further structural modifications of **AG-120** will set the stage for further

Table 1 AG-120 structural analogs and their ICOS/ICOSL inhibitory profiles based on the ICOS/ICOSL TR-FRET assay

Compound	TR-FRET IC_{50} (μM) of ICOS/ICOSL
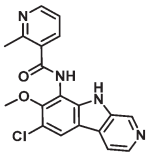 AG-120	12.24 ± 0.87
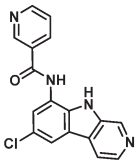 AG-120-I	13.89 ± 0.58
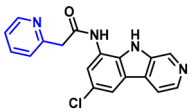 AG-120-II	37.14 ± 2.41
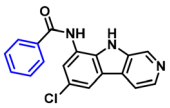 AG-120-III	>50
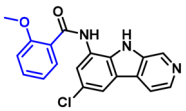 AG-120-IV	43.67 ± 3.18
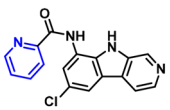 AG-120-V	28.64 ± 1.35
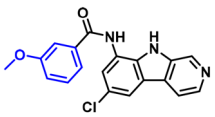 AG-120-VI	36.73 ± 2.03
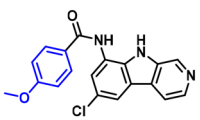 AG-120-VII	49.35 ± 3.74
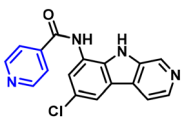 AG-120-VIII	31.04 ± 1.82
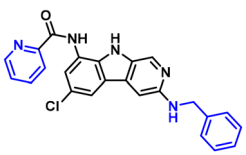 AG-120-IX	15.51 ± 1.06
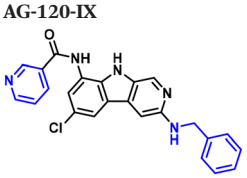 AG-120-X	4.68 ± 0.47

Table 1 *(continued)*

Compound	TR-FRET IC_{50} (μM) of ICOS/ICOSL
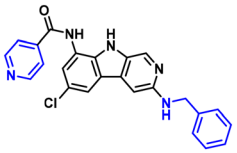 AG-120-XI	18.35 ± 0.91
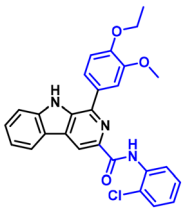 AG-120-XII	>50
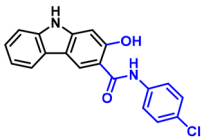 AG-120-XIII	>50
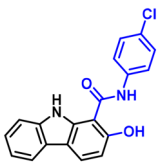 AG-120-XIV	>50
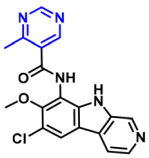 AG-120-XV	5.65 ± 0.13
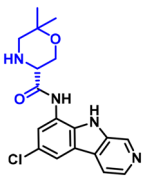 AG-120-XVI	11.08 ± 0.52

preclinical evaluation of the optimized small molecule inhibitors of ICOS/ICOSL interaction in animal models for immuno-oncology.

Experimental

ICOS/ICOSL TR-FRET assay

For the TR-FRET assay, we obtained human ICOS (NP_036224.1) extracellular domain (ECD) (Met1–Phe141) expressed with the Fc region of human IgG1 at the C-terminus from SinoBiological (Cat #10344-H02H). We procured ICOSL (NP_056074.1) ECD (Met1–Ser258) with a fused polyhistidine tag at the C-terminus from SinoBiological (Cat #11559-H08H). Both terbium (Tb) cryptate gold labeled anti-His mAb and XL665 labeled

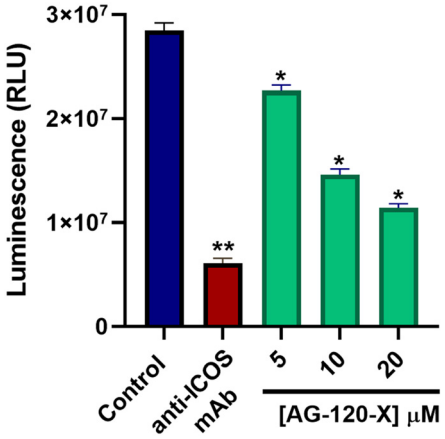

Fig. 6 Luminescence signal in co-cultures of ICOS effector cells and ICOSL/CHO-K1 cells (Promega ICOS blockade assay) upon co-incubation with anti-ICOS mAb (100 nM) or varying concentrations of **AG-120-X**. Error bars represent standard deviation (n = 3), (*p < 0.01, **p < 0.001 relative to untreated control).

anti-human mAb were obtained from Cisbio (part of PerkinElmer). TR-FRET measurements were done on the Tecan Infinite M1000 Pro. (Donor Read-620): excitation wavelength 340 nm/20 nm, emission wavelength 620 nm/10 nm, (Acceptor Read665): excitation wavelength 340 nm/20 nm, emission wavelength 665 nm/10 nm; both with 100 flashes per well, 500 ms integration time, 60 ms lag time. The assay mixture (18 μL) was immediately mixed prior to the assay to a final concentration of: ICOS (10 nM), ICOSL (10 nM), Tb cryptate labeled anti-His mAb (1 nM), and XL665 labeled anti-human Ab (10 nM). Stock solutions of tested compounds in DMSO (0.1%) and phosphate-buffered solution (PBS, pH 7.4) from the chemical library were applied to assay plates (medium binding white plates, Greiner #784075) at a final concentration (50 μM, n = 3). The assay mixture (18 μL) was added to the plated compounds (2 μL) and incubated for 1 h at room temperature. Measurements were performed as described above, and TR-FRET signals were calculated as a ratio as follows: (intensity of 665 nm)/(intensity of 620 nm) × 100. All assay plates contained control wells (n = 3) that include DMSO (0.1%) and wells that include all assay components except for Tag 2 (n = 3). Percent inhibition was calculated on a scale of 0% (*i.e.*, activity with DMSO vehicle only) to 100% (1 μM anti-ICOS mAb) using a full column of controls on each plate. The assay was performed in triplicate in a single run. The interquartile mean of control wells was used to calculate the Z' factor.

Hit identification: (1) we identified hits as compounds that result in 50% inhibition of the TR-FRET signal. (2) Fluorescent attenuators were identified using an additional readout of donor channel fluorescence data. Changes in donor fluorescence that mirror or contribute to overall activity (ratio of FRET/donor) indicate assay interference, and these compounds were not identified as hits.

Validation of the TR-FRET ICOS/ICOSL assay for HTS

The equation below was used to calculate the Z' factor:[58]

$$Z'\text{ factor} = 1 - \frac{(\text{S.D.} + \text{ve}) + (\text{S.D.} - \text{ve})}{(\text{mean} + \text{ve}) - (\text{mean} - \text{ve})}$$

where S.D. +ve: standard deviation for the positive control; S. D. −ve: standard deviation for the negative control; mean +ve: mean of the positive controls; mean −ve: mean of the negative controls. This experiment was performed in triplicate in 10 independent runs.

HPLC purity. AG-120 and structural analogs were obtained from established vendors, such as MedChemExpress, LabNetwork Chemicals, and Aurora Fine Chemicals. The purity of the compounds was confirmed to be >95% using HPLC analysis with the reverse-phase column Phenomenex Gemini, C18 (250 mm × 4.60 mm, 5 μm) on a HPLC Agilent system. The mobile phase used was acetonitrile–H_2O gradient with a 1 mL min^{-1} flow rate. UV absorption at 210 and 254 nm was used for monitoring the method.

ICOS/ICOSL ELISA. We procured the ICOS/ICOSL ELISA kit from BPS Bioscience (Catalog #79673) and performed the assay according to the manufacturer's recommended protocol using anti-ICOS antagonist mAb as a positive control. The assay was performed in triplicate in a single run.

ICOS/ICOSL blockade cell-based assay. We procured the ICOS/ICOSL blockade cell-based assay from Promega (Catalog #JA6001) and performed the assay according to the manufacturer's recommended protocol by co-culturing ICOS effector cells and ICOSL/CHO-K1 cells using anti-ICOS antagonist mAb as a positive control. The assay was performed in triplicate in a single run.

Computational studies

System setup. The X-ray structure of ICOS bound to ICOSL was obtained from Protein Data Bank (**https://www.rcsb.org/**) as available under PDB ID: 6 × 4 g.[61] The missing parts of the ICOS protein, *i.e.*, amino acid residues located between positions 22–30 and 129–130 were added based on their positions determined in the analogous crystal structure of ICOS in complex with anti-ICOS antibody (PDB ID: 7joo). Both structures were overlaid using the DALI server[67] (as shown in Fig. S4 of the ESI†). Based on this overlay the missing parts of the protein were constructed, and the following residues: Ile22, Gln23, Gly24, Ser25, Ala26, Asn27, Tyr28, Glu29 as well as His129 and Ile130 were added at N-termini and C-termini, respectively. The newly constructed ICOS–ICOSL complex model was subsequently used to compute pK_a shifts for titratable residues present in both proteins. The pK_a results were determined using PropKa ver. 3.0 software[68,69] and indicated that all residues are in their standard protonation states. After geometrical inspection, all histidine residues, *i.e.* His84, His101, His103, and His129 in ICOS as well as His112 and His147 of ICOSL were protonated at the δ-position, while His66 and His133 of ICOSL were

protonated at the ε-position. The existence of four disulfide bridges was established between Cys42 and Cys109, Cys63 and Cys83 in ICOS structure, and between Cys128 and Cys204 and Cys246 and Cys303 in ICOSL, therefore no hydrogen atoms were assigned to bind to S^{γ} atoms of these residues. Missing hydrogen atoms were added accordingly to both proteins.

Docking studies. Blind molecular docking was done using AutoDock Vina ver.1.2.0 (ref. 70 and 71) open-source software by employing MGLTools ver. 1.5.7.[72] Missing parameters such as atom types and atom charges for **AG-120**, as well as oligosaccharides present in structures of ICOS and ICOS-L were automatically generated using options directly provided by the program. Missing atom charges were assigned based on the Kollman charges[73] used as template values for each amino acid, whereas the Gasteiger charges[74] determined on the basis of electronegativity equilibration were computed by AutoDock Tools for the ligand and atypical residues present in the protein structures such as N-linked glycans.

Molecular dynamics simulations. A crystal structure of ICOS with the docked inhibitor was used as an initial model for molecular dynamics (MD) simulations at the molecular mechanics (MM) level. AMBER force field (FF)[75] parameters for standard amino acid residues were obtained from protein.ff14SB[76] FF, water, and counterions parameters were adapted from water.tip3p[77] FF, and finally parameters for non-standard Asn residues with N-linked glycan and N-linked two *N*-acetyl glucosamine (GlcNAc) and three mannose residues of the N-linked glycan at position 110 were obtained from GLYCAM_06j-1 (ref. 78) FF. Subsequently, missing AMBER FF parameters for the ligand were generated with a Generalized Amber Force Field (GAFF)[79] using the Antechamber software.[80] All newly assigned parameters are provided in Table S1 of the ESI.† Missing hydrogen atoms were added to the enzyme and substrate together with 3 negatively charged chloride (Cl^-) counterions that were put in the most electrostatically favorable positions to neutralize the total negative charge of the system. Hydrogen and counterions were added using the tLEAP[81] module of the AmberTools package. Subsequently, the system was soaked within an orthorhombic box of TIP3P water molecules, with an average size of 62 × 59 × 76 $Å^3$. NAMD software[82] was used as an MD engine. A cut-off for non-bonding interactions was set between 14.5 and 16 Å using a smooth switching function. The temperature during the simulations was controlled using the Langevin thermostat,[83] and the pressure with the Nosé–Hoover Langevin piston[84] pressure control. In all simulations, periodic boundary conditions (PBC) were applied. The equilibration and MD simulations were carried out following our standard computational protocol[85,86] and it involved a preliminary minimization and gradual heating of the system to 300 K with 0.001 K temperature increments, followed by 100 ps of non-biased NPT equilibration. The last generated structure in this step was then used as a starting geometry for 100 ns of no-restricted MD simulations. Due to the possible bias of starting point generated by the substrate position, free independent replicas of 100 ns of no-restricted NPT MD simulations were done and obtained results were analyzed using the cpptraj program.[87]

Conflicts of interest

There are no conflicts to declare.

Acknowledgements

We gratefully acknowledge financial support from the Spanish Ministry: Ministerio de Ciencia y Universidades (PID2019-107098RJ-I00) and Generalitat Valenciana (CIPROM/2021/079 and SEJI/2020/007). K. Ś. thanks Ministerio de Ciencia e Innovación and Fondo Social Europeo for her Ramon y Cajal contract (REF: RYC2020-030596-I).

Notes and references

1 Y. Zhang and Z. Zhang, The history and advances in cancer immunotherapy: understanding the characteristics of tumor-infiltrating immune cells and their therapeutic implications, *Cell. Mol. Immunol.*, 2020, **17**, 807–821.
2 Y. Shiravand, F. Khodadadi, S. M. Kashani, S. R. Hosseini-Fard, S. Hosseini, H. Sadeghirad, R. Ladwa, K. O'Byrne and A. Kulasinghe, Immune checkpoint inhibitors in cancer therapy, *Curr. Oncol. Rep.*, 2022, **29**, 3044–3060.
3 A. C. Huang and R. Zappasodi, A decade of checkpoint blockade immunotherapy in melanoma: understanding the molecular basis for immune sensitivity and resistance, *Nat. Immunol.*, 2022, **23**, 660–670.
4 J. A. Seidel, A. Otsuka and K. Kabashima, Anti-PD-1 and anti-CTLA-4 therapies in cancer: Mechanism of action, efficacy, and limitations, *Front. Oncol.*, 2018, **8**, 86.
5 Y. K. Chae, A. Arya, W. Iams, M. R. Cruz, S. Chandra, J. Choi and F. Giles, Current landscape and future of dual anti-CTLA4 and PD-1/PD-L1 blockade immunotherapy in cancer; lessons learned from clinical trials with melanoma and non-small cell lung cancer (NSCLC), *J. Immunother. Cancer*, 2018, **6**, 39.
6 A. J. Schoenfeld and M. D. Hellmann, Acquired Resistance to Immune Checkpoint Inhibitors, *Cancer Cell*, 2020, **37**, 443–455.
7 R. W. Jenkins, D. A. Barbie and K. T. Flaherty, Mechanisms of resistance to immune checkpoint inhibitors, *Br. J. Cancer*, 2018, **118**, 9–16.
8 L. Barrueto, F. Caminero, L. Cash, C. Makris, P. Lamichhane and R. R. Deshmukh, Resistance to Checkpoint Inhibition in Cancer Immunotherapy, *Transl. Oncol.*, 2020, **13**, 100738.
9 B. Zhou, Y. Gao, P. Zhang and Q. Chu, Acquired Resistance to Immune Checkpoint Blockades: The Underlying Mechanisms and Potential Strategies, *Front. Immunol.*, 2021, **12**, 693609.
10 D. J. Zahavi and L. M. Weiner, Targeting Multiple Receptors to Increase Checkpoint Blockade Efficacy, *Int. J. Mol. Sci.*, 2019, **20**, 158.

11 P. Sharma and J. P. Allison, Immune checkpoint targeting in cancer therapy: toward combination strategies with curative potential, *Cell*, 2015, **161**, 205–214.
12 C. Solinas, A. Gombos, S. Latifyan, M. Piccart-Gebhart, M. Kok and L. Buisseret, Targeting immune checkpoints in breast cancer: an update of early results, *ESMO Open*, 2017, **2**, e000255.
13 R. J. Davis, R. L. Ferris and N. C. Schmitt, Costimulatory and coinhibitory immune checkpoint receptors in head and neck cancer: unleashing immune responses through therapeutic combinations, *Cancers Head Neck*, 2016, **1**, 12.
14 C. Wang, H. Feng, X. Cheng, K. Liu, D. Cai and R. Zhao, Potential Therapeutic Targets of B7 Family in Colorectal Cancer, *Front. Immunol.*, 2020, **11**, 681.
15 J. Leung and W. K. Suh, The CD28-B7 Family in Anti-Tumor Immunity: Emerging Concepts in Cancer Immunotherapy, *Immune Netw.*, 2014, **14**, 265–276.
16 D. Capece, D. Verzella, M. Fischietti, F. Zazzeroni and E. Alesse, Targeting costimulatory molecules to improve antitumor immunity, *J. Biomed. Biotechnol.*, 2012, **2012**, 926321.
17 P. Greaves and J. G. Gribben, The role of B7 family molecules in hematologic malignancy, *Blood*, 2013, **121**, 734–744.
18 S. Jeong and S. H. Park, Co-Stimulatory Receptors in Cancers and Their Implications for Cancer Immunotherapy, *Immune Netw.*, 2020, **20**, e3.
19 G. Suntharalingam, M. R. Perry and S. Ward, *et al.*, Cytokine storm in a phase 1 trial of the anti-CD28 monoclonal antibody TGN1412, *N. Engl. J. Med.*, 2006, **355**, 1018–1028.
20 J. Zhang, Y. Zhang, B. Qu, H. Yang, S. Hu and X. Dong, If small molecules immunotherapy comes, can the prime be far behind?, *Eur. J. Med. Chem.*, 2021, **218**, 113356.
21 C. M. Lee and I. F. Tannock, The distribution of the therapeutic monoclonal antibodies cetuximab and trastuzumab within solid tumors, *BMC Cancer*, 2010, **10**, 255.
22 A. M. Scott, J. D. Wolchok and L. J. Old, Antibody therapy of cancer, *Nat. Rev. Cancer*, 2012, **12**, 278–287.
23 K. Imai and A. Takaoka, Comparing antibody and small-molecule therapies for cancer, *Nat. Rev. Cancer*, 2006, **6**, 714–727.
24 I. Hernandez, S. Bott and A. S. Patel, *et al.*, Pricing of monoclonal antibody therapies: higher if used for cancer?, *Am. J. Manag. Care*, 2018, **24**, 109–112.
25 M. Centanni, D. J. Moes, I. F. Trocóniz, J. Ciccolini and J. G. van Hasselt, Clinical Pharmacokinetics and Pharmacodynamics of Immune Checkpoint Inhibitors, *Clin. Pharmacokinet.*, 2019, **58**, 835–857.
26 A. Sosa, E. Cadena, C. Olive, N. Karachaliou and R. Rosell, Clinical assessment of immune-related adverse events, *Ther. Adv. Med. Oncol.*, 2018, **10**, 1758835918764628.
27 J. T. Ryman and B. Meibohm, Pharmacokinetics of Monoclonal Antibodies, *CPT: Pharmacometrics Syst. Pharmacol.*, 2017, **6**, 576–588.
28 W. Kerr and J. Chisholm, The next generation of immunotherapy for cancer: Small molecules could make big waves, *J. Immunol.*, 2019, **202**, 11–19.
29 A. Hutloff, A. M. Dittrich and K. C. Beier, *et al.*, ICOS is an inducible T-cell co-stimulator structurally and functionally related to CD28, *Nature*, 1999, **397**, 263–266.
30 V. Redoglia, U. Dianzani and J. M. Rojo, *et al.*, Characterization of H4: a mouse T lymphocyte activation molecule functionally associated with the CD3/T cell receptor, *Eur. J. Immunol.*, 1996, **26**, 2781–2789.
31 A. H. Sharpe and G. J. Freeman, The B7-CD28 superfamily, *Nat. Rev. Immunol.*, 2002, **2**, 116–126.
32 D. J. Wikenheiser and J. S. Stumhofer, ICOS Co-Stimulation: Friend or Foe?, *Front. Immunol.*, 2016, **7**, 304.
33 M. M. Swallow, J. J. Wallin and W. Sha, B7h, a novel costimulatory homolog of B7.1 and B7.2, is induced by TNFalpha, *Immunity*, 1999, **11**, 423–432.
34 S. Khayyamian, A. Hutloff and K. Büchner, *et al.*, ICOS-ligand, expressed on human endothelial cells, costimulates Th1 and Th2 cytokine secretion by memory CD4+ T cells, *Proc. Natl. Acad. Sci. U. S. A.*, 2002, **99**, 6198–6203.
35 T. Ito, S. Hanabuchi and Y. H. Wang, *et al.*, Two functional subsets of FOXP3+ regulatory T cells in human thymus and periphery, *Immunity*, 2008, **28**, 870–880.
36 M. Frydrychowicz, M. Boruczkowski, A. Kolecka-Bednarczyk and G. Dworacki, The Dual Role of Treg in Cancer, *Scand. J. Immunol.*, 2017, **86**, 436–443.
37 R. A. Peterson, Regulatory T-cells: diverse phenotypes integral to immune homeostasis and suppression, *Toxicol. Pathol.*, 2012, **40**, 186–204.
38 F. Amatore, L. Gorvel and D. Olive, Role of Inducible Co-Stimulator (ICOS) in cancer immunotherapy, *Expert Opin. Biol. Ther.*, 2020, **20**, 141–150.
39 J. Cinier, M. Hubert and L. Besson, *et al.*, Recruitment and Expansion of Tregs Cells in the Tumor Environment-How to Target Them?, *Cancers*, 2021, **13**, 1850.
40 Y. Burmeister, T. Lischke and A. C. Dahler, *et al.*, ICOS controls the pool size of effector-memory and regulatory T cells, *J. Immunol.*, 2008, **180**, 774–782.
41 M. Gobert, I. Treilleux and N. Bendriss-Vermare, *et al.*, Regulatory T cells recruited through CCL22/CCR4 are selectively activated in lymphoid infiltrates surrounding primary breast tumors and lead to an adverse clinical outcome, *Cancer Res.*, 2009, **69**, 2000–2009.
42 J. Faget, N. Bendriss-Vermare and M. Gobert, *et al.*, ICOS-ligand expression on plasmacytoid dendritic cells supports breast cancer progression by promoting the accumulation of immunosuppressive CD4+ T cells, *Cancer Res.*, 2012, **72**, 6130–6141.
43 N. Martin-Orozco, Y. Li and Y. Wang, *et al.*, Melanoma cells express ICOS ligand to promote the activation and expansion of T-regulatory cells, *Cancer Res.*, 2010, **70**, 9581–9590.
44 L. Strauss, C. Bergmann, M. Szczepanski, S. Lang, J. Kirkwood and T. L. Whiteside, Expression of ICOS on human melanoma-infiltrating $CD4^{+}CD25highFoxp3^{+}$ T

regulatory cells: implications and impact on tumor-mediated immune suppression, *J. Immunol.*, 2008, **180**, 2967–2980.

45 C. Conrad, J. Gregorio and Y. H. Wang, *et al.*, Plasmacytoid dendritic cells promote immunosuppression in ovarian cancer via ICOS costimulation of Foxp3(+) T-regulatory cells, *Cancer Res.*, 2012, **72**, 5240–5249.

46 X. M. Huang, X. S. Liu and X. Lin, *et al.*, Role of plasmacytoid dendritic cells and inducible costimulator-positive regulatory T cells in the immunosuppression microenvironment of gastric cancer, *Cancer Sci.*, 2014, **105**, 150–158.

47 Q. Chen, L. Mo and X. Cai, *et al.*, ICOS signal facilitates Foxp3 transcription to favor suppressive function of regulatory T cells, *Int. J. Med. Sci.*, 2018, **15**, 666–673.

48 H. Xu, X. Li and D. Liu, *et al.* Follicular T-helper cell recruitment governed by bystander B cells and ICOS-driven motility, *Nature*, 2013, **496**, 523–527.

49 D. Liu, H. Xu and C. Shih, *et al.*, T-B-cell entanglement and ICOSL-driven feed-forward regulation of germinal centre reaction, *Nature*, 2015, **517**, 214–218.

50 S. E. Yoon, J. Cho and Y. J. Kim, *et al.*, Comprehensive analysis of clinical, pathological, and genomic characteristics of follicular helper T-cell derived lymphomas, *Exp. Hematol. Oncol.*, 2021, **10**, 33.

51 M. J. Ahearne, R. L. Allchin, C. P. Fox and S. D. Wagner, Follicular helper T-cells: expanding roles in T-cell lymphoma and targets for treatment, *Br. J. Haematol.*, 2014, **166**, 326–335.

52 S. Chiba and M. Sakata-Yanagimoto, Advances in understanding of angioimmunoblastic T-cell lymphoma, *Leukemia*, 2020, **34**, 2592–2606.

53 M. A. Lunning and J. M. Vose, Angioimmunoblastic T-cell lymphoma: the many-faced lymphoma, *Blood*, 2017, **129**, 1095–1102.

54 R. Dobson, P. Y. Du and L. Rásó-Barnett, *et al.*, Early detection of T-cell lymphoma with T follicular helper phenotype by RHOA mutation analysis, *Haematologica*, 2022, **107**, 489–499.

55 J. C. Chavez, F. M. Foss and B. M. William, *et al.*, A Phase I Study of Anti-ICOS Antibody MEDI-570 for Relapsed/Refractory (R/R) Peripheral T-Cell Lymphoma (PTCL) and Angioimmunoblastic T-Cell Lymphoma (AITL) (NCI-9930), *Blood*, 2020, **136**, 5–6.

56 A. Broccoli and P. L. Zinzani, Emerging New Small Molecules in Peripheral T-cell Lymphomas, in *The Peripheral T-Cell Lymphomas*. Published online April 26, 2021, pp. 343–349.

57 M. T. Gabr and S. S. Gambhir, Discovery and Optimization of Small-Molecule Ligands for V-Domain Ig Suppressor of T-Cell Activation (VISTA), *J. Am. Chem. Soc.*, 2020, **142**, 16194–16198.

58 J. H. Zhang, T. D. Chung and K. R. Oldenburg, A Simple Statistical Parameter for Use in Evaluation and Validation of High Throughput Screening Assays, *J. Biomol. Screening*, 1999, **4**, 67–73.

59 C. A. Lipinski, F. Lombardo, B. W. Dominy and P. J. Feeney, Experimental and computational approaches to estimate solubility and permeability in drug discovery and development settings, *Adv. Drug Delivery Rev.*, 1997, **23**, 3–25.

60 J. B. Baell and G. A. Holloway, New substructure filters for removal of pan assay interference compounds (PAINS) from screening libraries and for their exclusion in bioassays, *J. Med. Chem.*, 2010, **53**, 2719–2740.

61 E. Rujas, H. Cui, T. Sicard, A. Semesi and J. P. Julien, Structural characterization of the ICOS/ICOS-L immune complex reveals high molecular mimicry by therapeutic antibodies, *Nat. Commun.*, 2020, **11**, 5066–5066.

62 S. Wang, G. Zhu, K. Tamada, L. Chen and J. Bajorath, Ligand binding sites of inducible costimulator and high avidity mutants with improved function, *J. Exp. Med.*, 2002, **195**, 1033–1041.

63 K. Świderek, I. Tuñón, I. H. Williams and V. Moliner, Insights on the origin of catalysis on glycine N-methyltransferase from computational modelling, *J. Am. Chem. Soc.*, 2018, **140**, 4327–4334.

64 R. J. Hall, C. W. Murray and M. L. Verdonk, The fragment network: A chemistry recommendation engine built using a graph database, *J. Med. Chem.*, 2017, **60**, 6440–6450.

65 P. Borysko, Y. Moroz, O. V. Vasylchenko and V. V. Hurmach, *et al.*, Straightforward hit identification approach in fragment-based discovery of bromodomain-containing protein 4 (BRD4) inhibitors, *Bioorg. Med. Chem.*, 2018, **26**, 3399–3405.

66 E. Sijbesma and E. Visser, *et al.*, Structure-based evolution of a promiscuous inhibitor to a selective stabilizer of protein-protein interactions, *Nat. Commun.*, 2020, **11**, 3954.

67 L. Holm, Dali server: structural unification of protein families, *Nucleic Acids Res.*, 2022, **50**, W210–W215.

68 C. R. Søndergaard, M. H. Olsson, M. Rostkowski and J. H. Jensen, Improved Treatment of Ligands and Coupling Effects in Empirical Calculation and Rationalization of pKa Values, *J. Chem. Theory Comput.*, 2011, **7**, 2284–2295.

69 M. H. Olsson, C. R. Søndergaard, M. Rostkowski and J. H. Jensen, PROPKA3: consistent treatment of internal and surface residues in empirical pKa predictions, *J. Chem. Theory Comput.*, 2011, **7**, 525–537.

70 J. Eberhardt, D. Santos-Martins, A. F. Tillack and S. Forli, AutoDock Vina 1.2.0: New Docking Methods, Expanded Force Field, and Python Bindings. Journal of Chemical Information and Modeling, *J. Chem. Inf. Model.*, 2021, **61**, 3891–3898.

71 O. Trott and A. J. Olson, AutoDock Vina: improving the speed and accuracy of docking with a new scoring function, efficient optimization and multithreading, *J. Comput. Chem.*, 2010, **31**, 455–461.

72 M. F. Sanner, Python: A Programming Language for Software Integration and Development, *J. Mol. Graphics Modell.*, 1999, **17**, 57–61.

73 U. C. Singh and P. A. Kollman, An approach to computing electrostatic charges for molecules, *J. Comput. Chem.*, 1984, **5**, 129–145.

74 J. Gasteiger and M. Marsili, Iterative partial equalization of orbital electronegativity-a rapid access to atomic charges, *Tetrahedron*, 1980, **36**, 3219–3228.

75 Y. Duan, C. Wu, S. Chowdhury, M. C. Lee, G. Xiong, W. Zhang, R. Yang, P. Cieplak, R. Luo and T. Lee, *et al.*, A point-charge force field for molecular mechanics simulations of proteins based on condensed-phase quantum mechanical calculations, *J. Comput. Chem.*, 2003, **24**, 1999–2012.

76 J. A. Maier, C. Martinez, K. Kasavajhala, L. Wickstrom, K. Hauser and C. Simmerling, ff14SB: Improving the Accuracy of Protein Side Chain and Backbone Parameters from ff99SB, *J. Chem. Theory Comput.*, 2015, **11**, 3696–3713.

77 W. L. Jorgensen, J. Chandrasekhar, J. D. Madura, R. W. Impey and M. L. Klein, Comparison of simple potential functions for simulating liquid water, *J. Chem. Phys.*, 1983, **79**, 926–935.

78 K. N. Kirschner, A. B. Yongye, S. M. Tschampel, J. González-Outeiriño, C. R. Daniels, B. Foley and R. J. Woods, GLYCAM06: A generalizable biomolecular force field. Carbohydrates, *J. Comput. Chem.*, 2008, **29**, 622–655.

79 J. Wang, R. M. Wolf, J. W. Caldwell, P. A. Kollman and D. A. Case, Development and testing of a general amber force field, *J. Comput. Chem.*, 2004, **25**, 1157–1174.

80 J. Wang, W. Wang, P. A. Kollman and D. A. Case, Automatic atom type and bond type perception in molecular mechanical calculations, *J. Mol. Graphics Modell.*, 2006, **25**, 247–260.

81 C. E. Schafmeister, W. S. Ross and V. Romanovski, *LEAP*, University of California, San Francisco, 1995.

82 J. C. Phillips, R. Braun, W. Wang, J. Gumbart, E. Tajkhorshid, E. Villa, C. Chipot, R. D. Skeel, L. Kalé and K. Schulten, Scalable molecular dynamics with NAMD, *J. Comput. Chem.*, 2005, **26**, 1781–1802.

83 G. S. Grest and K. Kremer, Molecular dynamics simulation for polymers in the presence of a heat bath, *Phys. Rev. A: At., Mol., Opt. Phys.*, 1986, **33**, 3628–3631.

84 G. J. Martyna, D. J. Tobias and M. L. Klein, Constant pressure molecular dynamics algorithms, *J. Chem. Phys.*, 1994, **101**, 4177–4189.

85 M. Gabr and K. Świderek, Discovery of a Histidine-Based Scaffold as an Inhibitor of Gut Microbial Choline Trimethylamine-Lyase, *ChemMedChem*, 2020, **15**, 2273–2279.

86 N. Serrano-Aparicio, V. Moliner and K. Świderek, Nature of Irreversible Inhibition of Human 20S Proteasome by Salinosporamide A. The Critical Role of Lys–Asp Dyad Revealed from Electrostatic Effects Analysis, *ACS Catal.*, 2021, **11**, 3575–3589.

87 D. R. Roe and T. E. Cheatham, PTRAJ and CPPTRAJ: Software for Processing and Analysis of Molecular Dynamics Trajectory Data, *J. Chem. Theory Comput.*, 2013, **9**, 3084–3095.